Image Enhancement in Active Incoherent Millimeter-Wave Imaging

Stavros Vakalis, Daniel Chen, Ming Yan, and Jeffrey A. Nanzer

Michigan State University, East Lansing, MI, USA

ABSTRACT

Active incoherent millimeter-wave imaging is an emerging technology that combines the benefits of passive and active millimeter-wave imaging by using incoherent noise transmission and passive receive interferometric processing. In this paper, we investigate computational image processing techniques to achieve enhanced image reconstruction with a small number of antenna elements and without the need for accurate calibration. We demonstrate enhancement of images through simulation and experimental data collected with a 38-GHz active incoherent millimeter-wave imager.

Keywords: Millimeter-wave imaging, computational imaging, incoherence, total variation, Haar wavelet, deconvolution

1. INTRODUCTION

Millimeter-wave imaging with improved resolution and real-time operation can benefit multiple applications, with the most prominent examples being contraband detection,[1,2] medical imaging,[3,4] remote sensing,[5] and non-destructive testing.[6] One inherent limitation that most current techniques face is slow imaging speed. This can be attributed to slow data acquisition because of mechanical rotations and scanning, or electrical scanning.[7] Computational microwave imaging can significantly reduce the data acquisition time and required number of antenna elements by employing image processing techniques and computational schemes. Computational imaging can be used for deblurring and noise reduction. Furthermore, computational imaging can also help mitigate hardware performance limitations.

Active incoherent millimeter-wave (AIM) imaging is a recently introduced technique that utilizes passive staring millimeter-wave imaging without the need for high sensitivity receivers. This is achieved with incoherent noise illumination from multiple transmit locations that mimic the properties of thermal radiation at a much higher signal-to-noise ratio (SNR). This approach has multiple advantages, including fast Fourier processing that can take place in real-time, sparse antenna arrays which lead to low system cost and are resistant to element failures, and no synchronization requirements between transmitters and receivers. Imaging resolution is inversely proportional to the maximum dimensions of the aperture, while image clarity depends on a number of factors, including hardware imperfections and system noise. In this work, we compensate for the coarse imaging resolution and low image quality that can be found in compact millimeter-wave arrays with a small number of elements and commercially available hardware. We focus on raw image reconstructions captured without array calibration, and use a computational imaging approach that is applicable in scenarios where accurate hardware calibration is not available. We use total variation (TV) and Haar wavelet regularization to deconvolve the image and simultaneously keep the image noise low. The sparsity of the Haar wavelets also maintain edge information. We measure the point spread function (PSF) of a 38-GHz experimental active incoherent millimeter-wave imaging system with a corner reflector in a semi-anechoic environment and deconvolve multiple imaging scenes to demonstrate the feasibility of our proposed technique.

Further author information: (Send correspondence to S.V. and J.N)
S.V.: E-mail: vakaliss@msu.edu
D.C.: E-mail: chendan7@msu.edu
M.Y.: E-mail: myan@msu.edu
J. N.: E-mail: nanzer@msu.edu

2. ACTIVE INCOHERENT MILLIMETER-WAVE IMAGING

Interferometric imaging was first developed in radio astronomy[8] where large antenna arrays observe the thermally generated electromagnetic radiation from stars and other stellar objects. More recently, it has been used for passive millimeter-wave imaging of humans and other objects.[9,10] The reason that most interferometric imaging systems are passive is related to the Van Cittert-Zernike theorem.[11] The theorem requires that the scene radiation should be spatio-temporally incoherent in order for the interferometric image reconstruction to succeed. This means that the phase response of every point in space should be largely random as a function of time. Thermal radiation is a result of random motions of atoms and molecules, hence by nature the phase in every spatial point of a thermally-radiating object is random. However, thermal radiation has very low power in millimeter-wave band, so passive interferometric systems require highly sensitive receive hardware that necessitates highly accurate calibration, combined with wide bandwidth and long integration times in order to detect the radiation. In contrast, active millimeter-wave imaging systems, which illuminate a scene with actively transmitted signals, do not suffer from these drawbacks, because of the relatively higher SNR obtained from the scattered signals. Nevertheless, most active millimeter-wave illuminations would not satisfy the incoherence requirement of the Van Cittert Zernike theorem because they employ coherent signals and every point in the scene would therefore generate highly correlated responses.

Active incoherent millimeter-wave imaging provides a novel way to mimic the incoherence of thermal radiation by illuminating the scene with random noise signals from multiple locations.[12,13] This retains all the benefits of passive interferometric arrays, such as sparsity and resistance to failures,[14,15] and the use of active signal transmission significantly boosts the received SNR and therefore mitigates the need for very high sensitivity.[16] Additional benefits include that there is no need for exact knowledge of the transmit fields in space, as is common in coherent computational imaging.[17]

Interferometric arrays sample the scene visibility $\mathcal{V}(u,v)$ which is the spatial Fourier transform of the scene intensity I. By performing pairwise cross-correlations on a sparse antenna array, samples of the scene visiblity $\mathcal{V}_s(u,v)$ are obtained. The discrete sampling of spatial frequencies can be represented in the above formulation through the use of a sampling function

$$S(u,v) = \sum_{m}^{M}\sum_{n}^{N} \delta(u-u_n)\delta(v-v_m), \tag{1}$$

where $N \cdot M$ is the maximum number of baselines, or spatial frequencies, realized by the array. The sampled visibility can be written as

$$\mathcal{V}_s(u,v) = S(u,v)\cdot\mathcal{V}(u,v). \tag{2}$$

The two-dimensional reconstructed scene intensity is then given by

$$I_r(\alpha,\beta) = \iint_{-\infty}^{\infty} \mathcal{V}_s(u,v) e^{-j2\pi(u\alpha+v\beta)} du dv \tag{3}$$

where $\alpha = \sin\theta\cos\phi$ and $\beta = \sin\theta\sin\phi$ are the direction cosines relative to u and v. The spatial frequency sampling process can be seen in terms of the scene intensity, and the spatial-domain response of the sampling function, which is the PSF of the array, and it is related to the sampling function in (1) through an inverse Fourier transform

$$PSF(\alpha,\beta) = \mathcal{F}^{-1}\{S(u,v)\}. \tag{4}$$

The PSF represents a synthesized beam in the spatial domain, and is defined by the baselines realized by the array. The output of the imaging process, the reconstructed image, is the convolution of the scene intensity and the PSF

$$I_r(\alpha,\beta) = PSF(\alpha,\beta) * I(\alpha,\beta), \tag{5}$$

where $*$ indicates convolution. From this formulation, it can be seen that the reconstructed image will be modified by the shape of the PSF. Eq. (5) is valid when the PSF is spatially invariant. This is not always the case, however for a narrow field of view broadside to the antenna array it is approximately true. The ideal PSF is a Dirac delta function $\delta(\alpha,\beta)$, however in practice it will consist of a main beam and a number of sidelobes because of the finite spatial bandwidth.

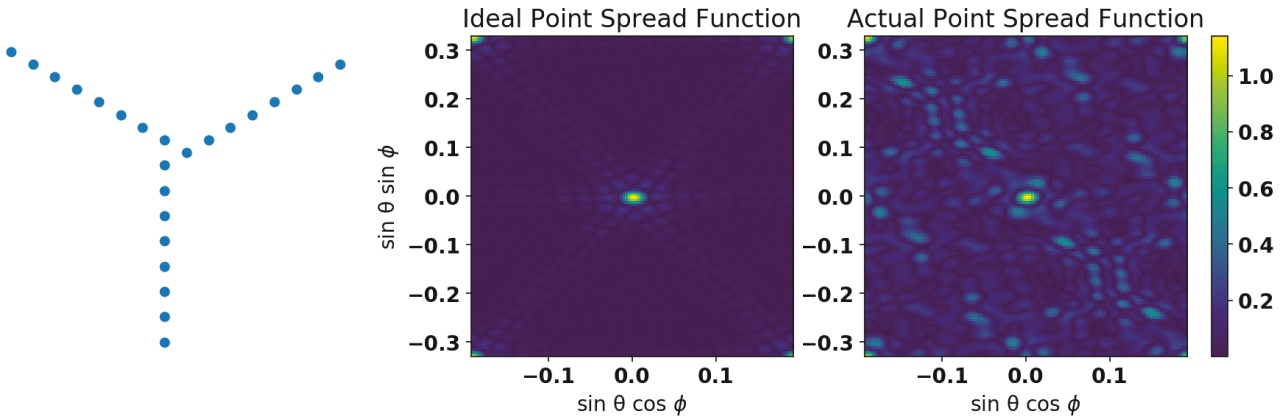

Figure 1. (left) Element locations of 24 element Y-shaped antenna array. (middle) Ideal point spread function of the 24-element array. The ambiguities on the edges can be mitigated by focusing on a narrower field of view. (right) Actual point spread function when introducing random amplitude and phase errors. The sidelobe level is significantly increased.

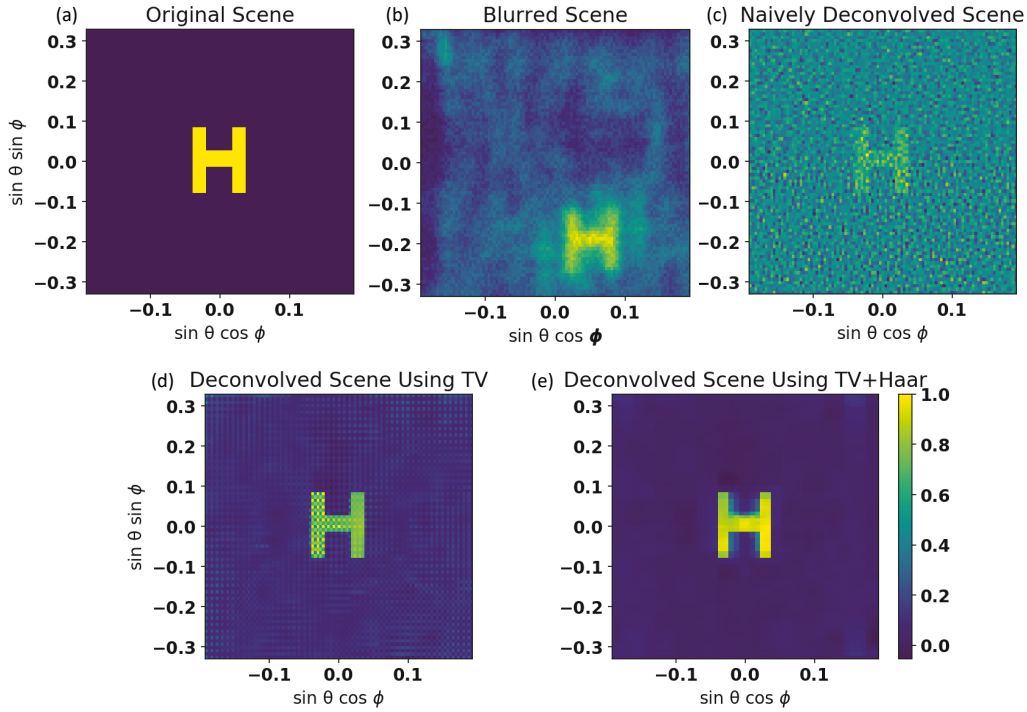

Figure 2. (a) Original scene. (b) Simulated millimeter-wave reconstruction with SNR=3.3 dB. The image appears shifted because of the random phase shifts in the PSF. (c) Deconvolved image using simple Fourier inversion of the Fourier transform of the PSF. The blurring is mitigated but the noise amplification effect is visible (RMSE= 0.62). (d) Deconvolved image using TV regularization. The blurring is mitigated, although not significantly, while higher frequency noise is smoothed out (RMSE = 0.07). (e) Deconvolved image using TV and Haar regularization. The Haar regularization has retained the edge information of the image, while the TV constraint has reduced noise significantly (RMSE = 0.06).

3. COMPUTATIONAL IMAGING FOR DECONVOLUTION

The PSF is usually used to characterize the blurring effect in the image reconstruction. A naive way to remove the blurring would be performing deconvolution by converting (5) in the spatial frequency domain and divide the Fourier transform of the reconstructed scene $\mathcal{V}_s$ with the Fourier transform of the PSF (i.e. $S(u, v)$). However, this is an ill-posed problem and would result in significant noise amplification. A regularizer function is needed to compensate for the lost information during the blurring.

The convolution based image formation from (5) can be turned into the general image reconstruction model

$$\mathbf{y} = \mathbf{A}\mathbf{x} + \mathbf{n}, \tag{6}$$

where $\mathbf{y}$ represents the reconstructed image samples from I_r, $\mathbf{A}$ is an operator modelling the blurring process from the PSF, $\mathbf{x}$ represents the true image samples from I, and $\mathbf{n}$ represents the image noise. An estimate of the reconstructed image $\hat{\mathbf{x}}$ can be obtained by

$$\min \quad L(\mathbf{x}) = \|\mathbf{y} - \mathbf{A}\mathbf{x}\|_2^2 + \lambda \mathrm{R}(\mathbf{x}), \tag{7}$$

where $\mathrm{R}(\mathbf{x})$ is the regularizer function and λ is the regularizer parameter. A very commonly used regularizer function for millimeter-wave images, which are piece-wise constant functions of reflectivity, is total variation $\mathrm{TV}(\mathbf{x})$

$$\mathrm{TV}(\mathbf{x}) = \sum_i \sqrt{(\Delta_i^H \mathbf{x})^2 + (\Delta_i^V \mathbf{x})^2} \tag{8}$$

where Δ_i^H and Δ_i^V are the finite differences operator along the horizontal and vertical dimension of x.[18,19] TV is also frequently used for denoising without the deconvolution.[20] Another commonly used regularizer function for deconvolution of images is the ℓ_1 norm $\|\cdot\|_1$ of the Haar wavelet transform. The Haar wavelet Ψ is a computationally efficient transform and widely used in image processing because it produces a sparse or approximately sparse matrix. The Haar wavelet regularizer can be written as

$$\min \quad \|\Psi\mathbf{x}\|_1 \tag{9}$$

In this work, we will be using TV regularizers along with the combination of TV and Haar wavelet. Haar wavelets are usually called "square" wavelets and can retain edge information in image reconstructions.[21]

4. SIMULATED COMPUTATIONAL IMAGING RECONSTRUCTIONS

Simulations were performed in Python using the PyLops toolbox.[22] The antenna locations synthesizing a 24-element Y-shaped array are shown in Fig. 1(left).[23] The simulated PSF of the Y-shaped array can be seen in Fig. 1(middle). The ambiguities on the edges of the PSF can be mitigated using a narrower circular window. The actual PSF when introducing random amplitude and phase errors can be seen in Fig. 1(right). Each antenna is characterized by a complex gain $G_i = e^{g_i + j\phi_i}$, where g_i is uniformly distributed in [-0.5,0.5] and ϕ_i is uniformly distributed in $[0,\pi]$. Using the actual PSF with random amplitude and phase errors, the simulations can be seen in Fig. 2. The original scene with an H-shaped target can be seen in Fig. 2(a). The blurred scene is a result of convolving the original scene with the actual PSF with random amplitude and phase errors plus noise. The SNR is 3.3 dB. Naively performing deconvolution by division in the spatial frequency domain amplifies the noise significantly. The root-mean-square error (RMSE) is 0.62. Deconvolving the scene using TV regularization gives significantly improved results in the noise suppression and achieves RMSE = 0.07. Adding the Haar wavelet sparsity constraint suppreses the noise even more and the rippling effect from simple TV regularization achieving RMSE = 0.06.

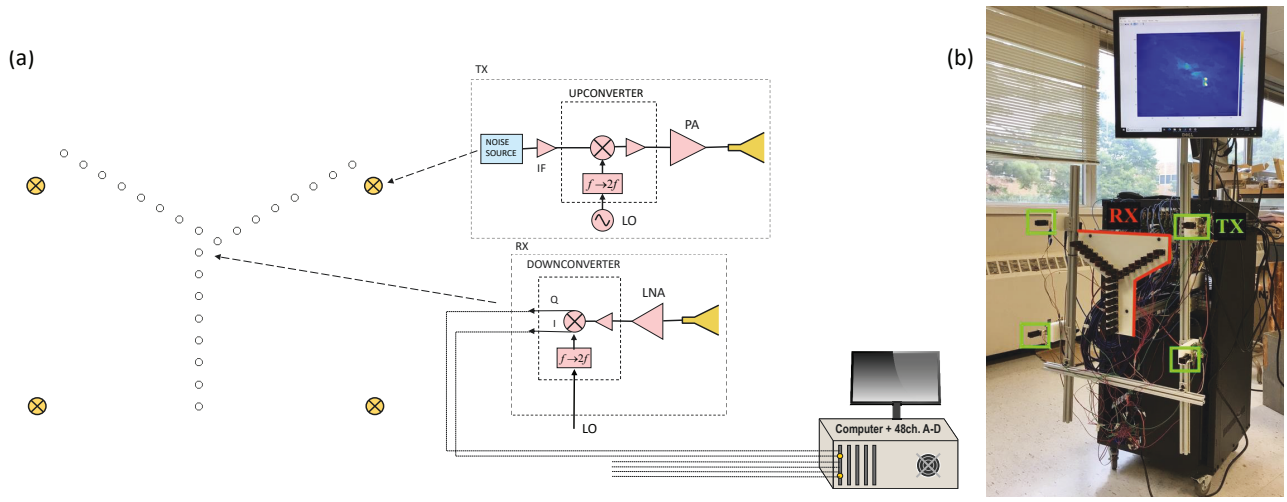

Figure 3. (a) Millimeter-wave digital array architecture used in the experimental measurements. Four noise transmitters are used in combination with 24 receivers. Each receive antenna response is digitized and all the processing takes place inside the host computer. (b) Photograph of the 38 GHz array. The transmitters (TX) are noted with green color while the receivers (RX) are noted with red color. All the digital hardware and the computer are placed inside the rack.

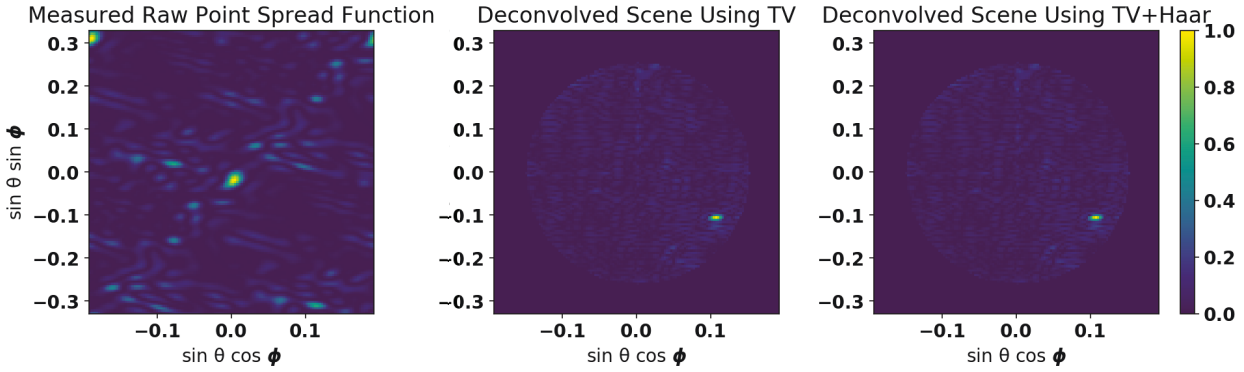

Figure 4. (left) Measured PSF using a corner reflector that provides a point-like response. (middle) Deconvolved reconstruction of a shifted response of the same corner in space using TV regularization. The result is a nice point like response. A circular mask is used to suppress the ambiguities at the edges of field of view. (right) Deconvolved reconstruction of a shifted response of the same corner in space using TV and Haar wavelet regularization. The result appears to be almost the same with the TV deconvolved scene.

5. EXPERIMENTAL COMPUTATIONAL IMAGING RECONSTRUCTIONS

Experimental measurements were conducted in a semi-anechoic environment. The system architecture that was used is shown in Fig. 3(a) and consisted of 24 receivers shaped in an asymmetric Y-shaped configuration and four noise transmitters placed outside the receiving array. Each received signal is downconverted to baseband and sampled using three ATS9416 - 14 bit, 100 MS/s, 16 channel digitizers. A photograph of the imager can be seen in Fig. 3(b). The 38 GHz receiving array is element-level digital, meaning that all processing of the signals received at each element occurs in the digital domain.

The 3D-printed receive antenna placement bracket had horizontal and vertical dimensions of 34 cm and 34 cm respectively. The horizontal and vertical spacings between the four transmitters were 56 cm and 49 cm,

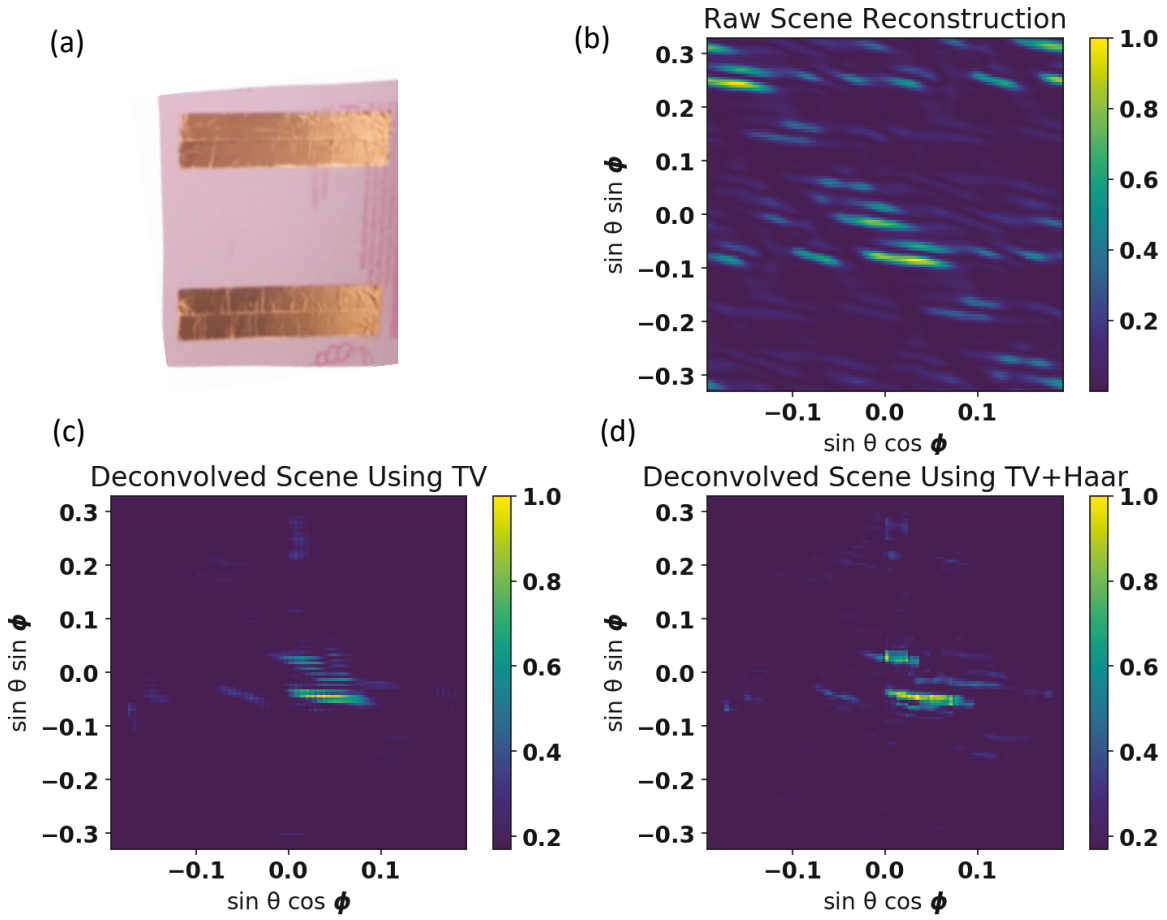

Figure 5. (a) Target with two reflecting stripes that was used in the experimental measurements. (b) Experimental raw scene reconstruction. (c) Deconvolved reconstruction of the scene using TV regularization. The artifacts have been suppressed significantly. A circular mask has been used. (d) Deconvolved reconstruction of the scene using TV and Haar wavelet regularization. The reconstruction appears improved compared to the TV reconstructed scene because of the edge information that the Haar wavelet can retain.

respectively. The transmitters consisted of 0.1-2 GHz calibrated noise sources with 15 dB excess noise ratio (ENR), that were upconverted to 38 GHz using Analog Devices (ADI) HMC6787A upconverters. At 38 GHz the noise signal was amplified using ADI HMC7229 power amplifiers. Both transmit and receive antennas were 15 dBi 3D-printed horn antennas that were fabricated at Michigan State University. For the receivers, each antenna was followed by a 20 dB gain ADI HMC1040 low-noise amplifier (LNA) before being downconverted to baseband using an ADI HMC6789 I/Q downconverter. A 19 GHz local oscillator (LO) was used for all the downconverters after being split into 24 ways.

The PSF was estimated using a large corner reflector, which acts as a strong point source. The "dirty" beam can be seen in Fig. 4 (left). Using the "dirty" beam we can perform deconvolution using TV regularization and the results can be seen in Fig. 4 (middle) for a a shifted corner reflector point source. A circular mask is used to filter the spatial ambiguities at the edges of the field of view. The noise has been suppressed and the response forms the desired shape of a sharp point. The results from the TV+Haar regularization can be seen in Fig. 4 (right). The results using TV or TV+Haar regularizers are minimally different for the single strong point target.

A target with two reflecting stripes was used which can be seen in Fig. 5(a). The distance between the two

stripes is 22 cm, while each stripe has dimensions of 10 by 38 cm. The "raw" reconstruction can be seen in Fig. 5(b). The deconvolved reconstruction using the TV constraint has significantly reduced the noise and the two stripes are visible in Fig. 5(c). The reconstruction is again multiplied with the circular mask. The deconvolved scene using TV + Haar regularization can be seen in Fig. 5(d). The edge information has been preserved due to the use of the "square" wavelet regularization.

6. CONCLUSION

The effect of computational imaging techniques was examined in this work in order to enhance the image reconstruction of active incoherent millimeter-wave systems. Although the transmitted radiation is not known, the PSF of the receive array can be estimated through a point source measurement using a corner reflector. The combination of TV and Haar Wavelet regularization demonstrates that a desirable overall performance can be achieved given the scenarios that no receiver calibration has been performed.

ACKNOWLEDGMENTS

The authors would like to thank Brian Wright from Michigan State University for his help with the experimental setup. This work was supported by the National Science Foundation under Grants ECCS-1708820 and DMS-2012439.

REFERENCES

[1] Appleby, R. and Wallace, H. B., "Standoff detection of weapons and contraband in the 100 ghz to 1 thz region," *IEEE Transactions on Antennas and Propagation* **55**(11), 2944–2956 (2007).

[2] Salmon, N. A., Mason, I., Wilkinson, P., Taylor, C., and Scicluna, P., "First imagery generated by near-field real-time aperture synthesis passive millimetre wave imagers at 94 GHz and 183 GHz," in [*Proc. SPIE Eur. Security + Defence, Millim. Wave, Terahertz Sens. Technol. III*], **7837**(01), 1–12 (2010).

[3] Aguilar, S. M., Al-Joumayly, M. A., Burfeindt, M. J., Behdad, N., and Hagness, S. C., "Multiband miniaturized patch antennas for a compact, shielded microwave breast imaging array," *IEEE Transactions on Antennas and Propagation* **62**(3), 1221–1231 (2014).

[4] Preece, A. W., Craddock, I., Shere, M., Jones, L., and Winton, H. L., "Maria m4: clinical evaluation of a prototype ultrawideband radar scanner for breast cancer detection," *Journal of Medical Imaging* **3**, 033502 (Jul 2016).

[5] Ruf, C. S., Swift, C. T., Tanner, A. B., and Le Vine, D. M., "Interferometric synthetic aperture microwave radiometry for the remote sensing of the earth," *IEEE Transactions on Geoscience and Remote Sensing* **26**(5), 597–611 (1988).

[6] Zidane, F., Lanteri, J., Marot, J., Brochier, L., Joachimowicz, N., Roussel, H., and Migliaccio, C., "Non-destructive control of fruit quality via millimeter waves and classification techniques: Investigations in the automated health monitoring of fruits," *IEEE Antennas and Propagation Magazine* **62**(5), 43–54 (2020).

[7] Hansen, R. C., [*Phased Array Antennas*], John Wiley and Sons (2002).

[8] Thompson, A. R., Moran, J. M., and Swenson, G. W., [*Interferometry and Synthesis in Radio Astronomy*], John Wiley and Sons (2001).

[9] Yujiri, L. and et al., "Passive millimeter-wave camera," in [*Passive Millimeter-Wave Imaging Technology*], Smith, R. M., ed., SPIE (Jun 1997).

[10] Nohmi, H., Ohnishi, S., and Kujubu, O., "Passive millimeter-wave camera with interferometric processing," in [*Passive Millimeter-Wave Imaging Technology X*], Appleby, R. and Wikner, D. A., eds., SPIE (Apr 2007).

[11] Born, M. and Wolf, E., [*Principles of optics*], Cambridge Univ. Pr. (1999).

[12] Vakalis, S., Gong, L., He, Y., Papapolymerou, J., and Nanzer, J. A., "Experimental demonstration and calibration of a 16-element active incoherent millimeter-wave imaging array," *IEEE Transactions on Microwave Theory and Techniques* **68**(9), 3804–3813 (2020).

[13] Vakalis, S. and Nanzer, J. A., "Microwave imaging using noise signals," *IEEE Transactions on Microwave Theory and Techniques* **66**(12), 5842–5851 (2018).

[14] Vakalis, S. and Nanzer, J. A., "Analysis of array sparsity in active incoherent microwave imaging," *IEEE Geoscience and Remote Sensing Letters* **17**(1), 57–61 (2020).

[15] Vakalis, S. and Nanzer, J. A., "Analysis of element failures in active incoherent microwave imaging arrays using noise signals," *IEEE Microwave and Wireless Components Letters* **29**(2), 161–163 (2019).

[16] Vakalis, S., Chen, D., and Nanzer, J. A., "Toward space–time incoherent transmitter design for millimeter-wave imaging," *IEEE Antennas and Wireless Propagation Letters* **19**(9), 1471–1475 (2020).

[17] Imani, M. F., Gollub, J. N., Yurduseven, O., Diebold, A. V., Boyarsky, M., Fromenteze, T., Pulido-Mancera, L., Sleasman, T., and Smith, D. R., "Review of metasurface antennas for computational microwave imaging," *IEEE Transactions on Antennas and Propagation* **68**(3), 1860–1875 (2020).

[18] Bioucas-Dias, J. M., Figueiredo, M. A. T., and Oliveira, J. P., "Total variation-based image deconvolution: a majorization-minimization approach," in [*2006 IEEE International Conference on Acoustics Speech and Signal Processing Proceedings*], **2**, II–II (2006).

[19] Combettes, P. L. and Pesquet, J., "Image restoration subject to a total variation constraint," *IEEE Transactions on Image Processing* **13**(9), 1213–1222 (2004).

[20] Coupe, P., Yger, P., Prima, S., Hellier, P., Kervrann, C., and Barillot, C., "An optimized blockwise nonlocal means denoising filter for 3-d magnetic resonance images," *IEEE Transactions on Medical Imaging* **27**(4), 425–441 (2008).

[21] Makowski, P. L., "Redundant haar wavelet regularization in sparse-view optical diffraction tomography of microbiological structures," in [*Speckle 2018: VII International Conference on Speckle Metrology*], Józwik, M., Jaroszewicz, L. R., and Kujawińska, M., eds., SPIE (Sep 2018).

[22] Ravasi, M. and Vasconcelos, I., "Pylops—a linear-operator python library for scalable algebra and optimization," *SoftwareX* **11**, 100361 (Jan 2020).

[23] Tanner, A. B., Wilson, W. J., Lambrigsten, B. H., Dinardo, S. J., Brown, S. T., Kangaslahti, P. P., Gaier, T. C., Ruf, C. S., Gross, S. M., Lim, B. H., Musko, S. B., Rogacki, S. A., and Piepmeier, J. R., "Initial results of the geostationary synthetic thinned array radiometer (geostar) demonstrator instrument," *IEEE Transactions on Geoscience and Remote Sensing* **45**(7), 1947–1957 (2007).